Beam Misalignments and Fluid Velocities

in Laser-Induced Thermal Acoustics (LITA)

Stefan Schlamp[*]   Eric B. Cummings[†]   Hans G. Hornung[‡]

February 5, 1999

Abstract

Beam misalignments and bulk fluid velocities can influence the time history and intensity of laser-induced thermal acoustics (LITA) signals. A closed-form analytic expression for LITA signals incorporating these effects is derived, allowing the magnitude of beam misalignment and velocity to be inferred from the signal shape. It is demonstrated how instantaneous, nonintrusive, and remote measurement of sound speed (temperature) and velocity (Mach number) can be inferred simultaneously from homodyne-detected LITA signals. The effects of different forms of beam misalignment are explored experimentally and compared with theory, with good agreement, allowing the amount of misalignment to be measured from the LITA signal. This capability could be used to correct experimental misalignments and account for the effects of misalignment in other LITA measurements. It it shown that small beam misalignments have no influence on the accuracy or repeatability of sound speed measurements with LITA.

Key words: four-wave mixing, velocimetry, transient grating, scattering, non-intrusive

OCIS codes: 000.2170 (Equipment and Techniques), 050.2770 (Gratings), 120.6780 (Temperature), 120.7280 (Velocimetry), 190.4380 (Four-Wave Mixing)

[*]Graduate Aeronautical Laboratories, California Institute of Technology, Pasadena, California 91125
[†]Sandia National Laboratories, Livermore, Califronia 94551
[‡]Graduate Aeronautical Laboratories, California Institute of Technology, Pasadena, California 91125

1 Introduction

The four-wave mixing technique Laser-Induced Thermal Acoustics is used in various laboratories to measure the sound speed and thermal diffusivity (e.g., Ref. [1]) as well as fluid velocities (e.g., Ref. [2], [3]). A grating-shaped pressure and temperature perturbation is created in a fluid by two coherent intersecting pulsed laser beams. These perturbations evolve hydrodynamically in time and space. This evolution can be examined by focusing a third continuous laser beam on the associated density gratings at its Bragg angle. Depending on the modulation depth of the density grating, a fraction of this source beam is coherently scattered into a weak signal beam. The induced acoustic waves move outwards, modulating the density field and hence the signal at the grating Brillouin frequency, or the frequency of sound waves with the grating wavelength. Hence, one approach to measure the sound speed is to measure the frequency of the signal modulation. However, finite signal lifetime and sampling resolution limits the accuracy of this technique.

Another approach is to model the physics of the interactions that produce the LITA signal and derive an analytic expression for the signal as a function of experimental parameters, fluid properties including the sound speed and thermal diffusivity, and fluid velocity. A least-squares fit of this expression to experimental signals then provides best estimates of the signal parameters and hence fluid properties. Cummings (Ref. [4]) derived such an expression that includes thermalization and electrostriction as the two main mechanisms for the creation of the grating. However the assumption was made that the system was in perfect optical alignment and that the fluid was at rest. Obviously this approach breaks down when these assumptions are grossly violated. In these cases, the theory is not a valid representation of the experiment and the fitting procedure returns erroneous values.

The work presented here extends the earlier theory to include the effects of a convection velocity and finite beam misalignment. These may then be measured through the least-squares fitting procedure, simplifying LITA velocimetry. Present velocimetry techniques using LITA rely on the measurement of a small Doppler shift of the signal beam using heterodyne detection. Now, only

2

from the recorded signal and using the simpler homodyne detection, sound speed, velocities and transport properties of the fluid can be extracted simultaneously. In addition we can extract beam misalignment measurements from the signal and either realign the optics with this information or take them into account in the data analysis.

In the first part of this paper, the LITA analysis of Ref. [4] is extended using nomenclature mostly adapted from that derivation. First, the grating creation due to the opto-acoustic forcing is modeled. The functional form of the electric field grating in the sample volume is derived. Next, the fluid response to the electric field is examined. Since the underlying physics have not changed, the fluid response to electric fields has been left unchanged from Ref. [4], only the results are given, and the interested reader is referred to there and to Ref. [5]. Finally, the scattering of the source beam into the signal beam is modeled using the linearized equation of light scattering.

In the second part, experimental results are presented that validate the theory.

2 Frame of Reference

We define our frame of reference so that the origin of our fixed Cartesian coordinate system is at the focus of the source beam as shown in Fig. 1. The source beam lies in the $x - y$-plane and forms an angle ψ with the x-axis. The $x - z$-plane bisects the two driver beams so that each one intersects this plane at an angle θ. They intersect the $x - y$-plane at angles ϕ_1 and ϕ_2 (angular misalignment). Their foci are at $\vec{r}_1$ and $\vec{r}_2$, respectively (spatial misalignment). We denote the time of the short driver pulse as $t = 0$.

3 Opto-Acoustic Forcing

We first model the electric field grating in the sample volume defined by the shallow-angle intersection of the two driver beams. Assume each driver laser beam has a Gaussian profile with Gaussian half-width ω and denote the normalized electric fields of the two driver lasers by $E_{d1}(\vec{r}, t)$ and
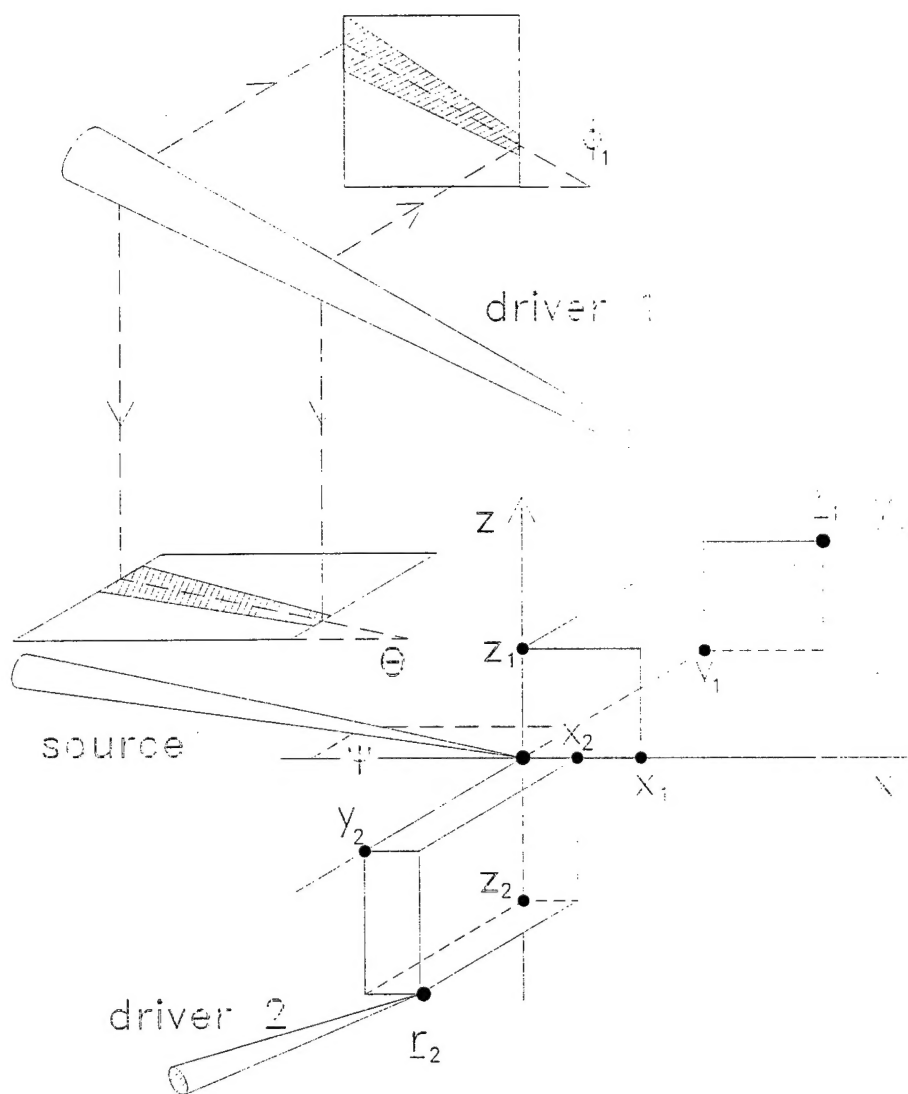
3

Figure 1: Frame of reference for LITA analysis.

THIS PAGE IS MISSING IN ORIGINAL DOCUMENT

5

E_d is the total energy of the driver laser field, $P_d(t)$ is the normalized driver laser intensity history, and I_d is the normalized grating intensity distribution. Terms neglected in Eqn. 2 only contribute a background intensity that will have no significant influence on the signal. The result for I_d is

$$I_d = \frac{2}{\pi\omega^2} \cos\{2k_d [-\xi\cos\theta + (y - \overline{\eta})\sin\theta]\}$$
$$\times \exp\left\{-\frac{2}{X^2}\left[x - \left(\overline{\xi} - \frac{X}{Y}\eta\right)\right]^2 - \frac{2}{Y^2}\left[y - \left(\overline{\eta} - \frac{Y}{X}\xi\right)\right]^2 - \frac{2}{Z^2}\left[\left(z - \overline{\zeta}\right)^2 + \zeta^2\right]\right\},$$

$$(3a)$$

where

$$
\begin{array}{lll}
X = \dfrac{\omega}{\sin\theta} & Y = \dfrac{\omega}{\cos\theta} & Z = \omega \\[2mm]
\overline{\xi} = (x_1 + x_2)/2 & \overline{\eta} = (y_1 + y_2)/2 & \overline{\zeta} = (z_1 + z_2)/2 \\[2mm]
\xi = (x_1 - x_2)/2 & \eta = (y_1 - y_2)/2 & \zeta = (z_1 - z_2)/2.
\end{array}
\qquad (3b)
$$

At this point we use the fact the the beam crossing angle is small and that hence the $X \gg Y, Z$. Consequently, we neglect all variations in the x-direction including the misalignments. The side effect of this assumption together with the assumption of no angular misalignments is that we exclude any rotation of the grating, i.e. it is always perpendicular to the y-direction. The proper limit of Eqn. 3a is then

$$I_d = \frac{2}{\pi\omega^2} \exp\left\{-\frac{2}{Y^2}\left[(y - \overline{\eta})^2 + \eta^2\right] - \frac{2}{Z^2}\left[\left(z - \overline{\zeta}\right)^2 + \zeta^2\right]\right\} \cos\{q_\psi(y - \overline{\eta})\} \qquad (4)$$

with $q_\psi = 2k_d \sin\theta$. Eqn. 4 represents a fringe pattern perpendicular to the y-direction with a Gaussian intensity profile centered at $(0, \overline{\eta}, \overline{\zeta})$.

At a later point we will have to take the 3-dimensional convolution of I_d with the Green's functions of the fluid response to the electric field. This operation will be performed by multiplying

6

THIS PAGE IS MISSING IN ORIGINAL DOCUMENT

H_e for the opto-acoustic response of the fluid to thermalization and electrostriction respectively, are

$$H_\theta(q,t) = H_{\theta P1}\Phi_{P1} + H_{\theta P2}\Phi_{P2} + H_{\theta T}\Phi_T + H_{\theta D}\Phi_D \tag{6a}$$

$$H_e(q,t) = H_{eP1}\Phi_{P1} + H_{eP2}\Phi_{P2} + H_{eT}\Phi_T. \tag{6b}$$

where

$$\Phi_{P1,2}(q,t) = \exp\left\{-\Gamma q^2 t \pm ic_s qt + ivtq_y + iwtq_z\right\}$$
$$\Phi_T(q,t) = \exp\left\{-D_T q^2 t + ivtq_y + iwtq_z\right\}$$
$$\Phi_D(q,t) = \exp\left\{-(\gamma_\theta + \gamma_{n\theta})t - D_s q^2 t + ivtq_y + iwtq_z\right\} \tag{6c}$$

$$H_{\theta P1} = \frac{[1 + i(\Delta - G)][1 - G\Pi - i\Pi]}{2[1 + (\Delta - G)^2][(1 - G\Pi)^2 + \Pi^2]} = H_{\theta P2}^*$$

$$H_{\theta T} = -\frac{1}{[1 + (\Delta - G)^2][1 - \Delta\Pi]} \qquad H_{\theta D} = \frac{\Pi^2}{[(1 - G\Pi)^2 + \Pi^2][1 - \Delta\Pi]}$$

$$H_{eP1} = i\frac{[1 - i(\gamma\Delta - G)][1 + i(\Delta - G)]}{2[1 + (\Delta - G)^2]} = H_{eP2}^* \qquad H_{eT} = \frac{(\gamma - 1)\Delta}{[1 + (\Delta - G)^2]}, \tag{6d}$$

and

$$\Pi = c_s q / (\gamma_\theta + \gamma_{n\theta} + D_s q^2). \tag{6e}$$

Δ is the thermal grating damping over a period of acoustic motion and Γ is the acoustic damping rate ($\Gamma = 1/2[(\gamma - 1)D_T + D_V]$). Π is the ratio of the sound wave frequency with the wave vector q_y to the excited state energy decay rate. γ is the ratio of specific heats, D_T the thermal diffusivity, D_V the longitudinal kinematic diffusivity of the fluid, and D_S the diffusivity of excited-state target molecules. γ_θ is the rate of excited-state energy decay caused by thermalization while $\gamma_{n\theta}$ is the energy decay rate not due to thermalization.

Φ_{P1} and Φ_{P2} are associated with the acoustic waves traveling in opposite directions, Φ_T is related to the density perturbations caused by the thermal grating, and Φ_D is due to the finite

8

thermalization rate. A single-rate thermalization process is assumed. The density-time behavior is then

$$\frac{\rho\prime(\vec{q}, t)}{\rho} = -\omega^2 I_d P_d(t) \circ [H_\theta U_\theta + H_e U_e] \tag{7}$$

where U_θ and H_e are the approximate modulation depths of the thermalization and the electrostriction grating respectively.

$I_d(\vec{q})$ is peaked at $\vec{q} = (0, q_\psi, 0)$. So, approximate to first order, $q \approx q_y$. This implies the assumption of plane wave fronts which is a good approximation if the waves have not traveled too far from their point of origin and if the fringe spacing is small. Also note that $q_z = 0$ implies a constant intensity in q_y-direction when in fact, the intensity has a Gaussian profile in this direction. But the error is only a multiplicative factor, since all grating cross sections perpendicular to q_z are self-similar.

Taking the inverse Fourier transform of the products

$$\Phi^{(d)}_{\{P1,P2,T,D\}} = I_d(\vec{q}) \Phi_{\{P1,P2,T,D\}}(\vec{q}, t), \tag{8}$$

we obtain:

$$\Phi^{(d)}_{P1,2}(\vec{r}, t) = \frac{2}{\pi\omega^2} \exp\left\{-\frac{2}{Y^2}\eta^2 - \frac{2}{Z^2}\zeta^2\right\} \exp\left\{-\Gamma q_\psi^2 t\right\} \cos\left\{(y - (v \pm c_s)t) q_\psi\right\}$$
$$\times \exp\left\{-\frac{2}{Y^2}[y - (\bar{\eta} + (v \pm c_s)t)]^2 - \frac{2}{Z^2}\left[z - \left(\bar{\zeta} + wt\right)\right]^2\right\} \tag{9a}$$

$$\Phi^{(d)}_{T}(\vec{r}, t) = \frac{2}{\pi\omega^2} \exp\left\{-\frac{2}{Y^2}\eta^2 - \frac{2}{Z^2}\zeta^2\right\} \exp\left\{-D_T q_\psi^2 t\right\} \cos\left\{(y - vt) q_\psi\right\}$$
$$\times \exp\left\{-\frac{2}{Y^2}[y - (\bar{\eta} + (v + c_s)t)]^2 - \frac{2}{Z^2}\left[z - \left(\bar{\zeta} + wt\right)\right]^2\right\} \tag{9b}$$

$$\Phi^{(d)}_{D}(\vec{r}, t) = \frac{2}{\pi\omega^2} \exp\left\{-\frac{2}{Y^2}\eta^2 - \frac{2}{Z^2}\zeta^2\right\} \exp\left\{-D_S q_\psi^2 t - (\gamma_\theta + \gamma_{n\theta})t\right\} \cos\left\{(y - vt) q_\psi\right\}$$
$$\times \exp\left\{-\frac{2}{Y^2}[y - (\bar{\eta} + (v + c_s)t)]^2 - \frac{2}{Z^2}\left[z - \left(\bar{\zeta} + wt\right)\right]^2\right\}. \tag{9c}$$

In Eqns. 9a-c, the assumption is made that the length scales do not change due to diffusion over the LITA time scales. Also, a phase shift of $\bar{\eta} q_\psi$ has been dropped in all three cosine terms.

5 Acousto-Optical Scattering

After describing the creation and time evolution of the density grating in the sample volume, the next step is to model how a continuous source beam focused at the origin and incident on the grating at the phase-matched angle ψ scatters off the grating into the coherent signal beam.

If we assume the density variations $\rho\prime$ to be small, we can use the linearized equation of light scattering (Ref. [8]). A narrow-band source beam $E_0(\vec{r}, t) \cos(\omega_0 t)$ scatters into the electric field E_s by a small disturbance in the susceptibility $\chi(\vec{r}, t; \omega)$. In the far field:

$$E_s(\vec{R}, t; \vec{q}) = -\frac{k_s^2}{4\pi R} \cos(\vec{k}_s \cdot \vec{R} - \omega_0 t)\mu(\vec{q}, t), \tag{10}$$

where k_s is the wave vector of the scattered beam, ω_0 is the frequency of the source beam, $\vec{R}$ is the position vector relative to the scatterer, and $\mu(\vec{q}, t)$ is the Fourier transform of the overlap of the susceptibility grating and the source laser field

$$\mu(\vec{r}, t) = \chi\prime(\vec{r}, t; \omega_0) E_0(\vec{r}, t). \tag{11}$$

Just as with the driver beams, assume the source beam to have spatially a Gaussian intensity profile. Hence,

$$\vec{E}_S = \vec{E}_0 + \vec{E}_0^* \tag{12a}$$

$$\vec{E}_0 = \frac{1}{2} \exp\{ik_0\hat{e}_0 \cdot \vec{r} - i\omega_0 t\} \exp\left\{-\left|\frac{\hat{e}_0 \times \vec{r}}{\sigma}\right|^2\right\} \tag{12b}$$

$$\hat{e}_0 = (\cos\psi, \sin\psi, 0). \tag{12c}$$

Proceeding as before with the driver lasers, the electric field of the source laser is $E_S(\vec{r}, t) = P_0(t)I_0(\vec{r})\cos(\omega_0 t)$ with

$$I_0 = \sqrt{\frac{2}{\pi\sigma^2}} \exp\left\{-\left(\frac{y}{\sigma_y}\right)^2 - \left(\frac{z}{\sigma_z}\right)^2\right\}, \tag{13a}$$

where σ is the Gaussian half-width of the source laser and

$$\sigma_y = \frac{\sigma}{\sin\psi} \qquad \sigma_z = \sigma. \tag{13b}$$

10

In Eqns. 13a,b variations in x-direction have been neglected by assuming $\sigma_x = \sigma/\sin\psi \gg \sigma_y, \sigma_z$. Define $\Phi^{(d,0)}_{\{P1,P2,T,D\}}(\vec{r},t) = I_0(\vec{r})\Phi^{(d)}_{\{P1,P2,T,D\}}$, the field of the overlap of the source beam and the evolving density grating. Taking the Fourier transform of these products, we can write

$$\Phi^{(d,0)}_{\{P1,P2,T,T\}}(\vec{q},t) = N\Psi_{\{P1,P2,T,T\}}(\vec{q};t)\Sigma_{\{P1,P2,T,T\}}(t) \tag{14a}$$

where

$$N = \frac{\sqrt{2/\pi}}{\sigma\omega^2}\left(\frac{Y^2\sigma_y^2}{Y^2+2\sigma_y^2}\right)^{1/2}\left(\frac{Z^2\sigma_z^2}{Z^2+2\sigma_z^2}\right)^{1/2}\exp\left\{-\frac{2}{Y^2}\eta^2 - \frac{2}{Z^2}\zeta^2\right\} \tag{14b}$$

$$\Psi_{P1,2} = \exp\left\{-\frac{1}{4}\frac{Y^2\sigma_y^2}{Y^2+2\sigma_y^2}(q_y-q_\psi)^2 + i\frac{2\sigma_y^2}{Y^2+2\sigma_y^2}(\overline{\eta}+(v\pm c_s)t)(q_y-q_\psi)\right\}$$

$$\times \exp\left\{-\frac{1}{4}\frac{Z^2\sigma_z^2}{Z^2+2\sigma_z^2}q_z^2 + i\frac{2\sigma_z^2}{Z^2+2\sigma_z^2}\left(\overline{\zeta}+wt\right)q_z\right\}$$

$$\Psi_T = \exp\left\{-\frac{1}{4}\frac{Y^2\sigma_y^2}{Y^2+2\sigma_y^2}(q_y-q_\psi)^2 + i\frac{2\sigma_y^2}{Y^2+2\sigma_y^2}(\overline{\eta}+vt)(q_y-q_\psi)\right\}$$

$$\times \exp\left\{-\frac{1}{4}\frac{Z^2\sigma_z^2}{Z^2+2\sigma_z^2}q_z^2 + i\frac{2\sigma_z^2}{Z^2+2\sigma_z^2}\left(\overline{\zeta}+wt\right)q_z\right\} = \Psi_D \tag{14c}$$

$$\Sigma_{P1,2} = \exp\left\{-\Gamma q_\psi^2 t - \frac{2(\overline{\eta}+(v\pm c_s)t)^2}{Y^2+2\sigma_y^2} - \frac{2}{Z^2+2\sigma_z^2}\left(\overline{\zeta}+wt\right)^2 + iq_\psi(v\pm c_s)t\right\}$$

$$\Sigma_T = \exp\left\{-D_T q_\psi^2 t - \frac{2(\overline{\eta}+vt)^2}{Y^2+2\sigma_y^2} - \frac{2\left(\overline{\zeta}+wt\right)^2}{Z^2+2\sigma_z^2} + iq_\psi vt\right\}$$

$$\Sigma_D = \exp\left\{-D_s q_\psi^2 t - (\gamma_\theta+\gamma_{n\theta})t - \frac{2(\overline{\eta}+vt)^2}{Y^2+2\sigma_y^2} - \frac{2\left(\overline{\zeta}+wt\right)^2}{Z^2+2\sigma_z^2} + iq_\psi vt\right\} \tag{14d}$$

In Eqn. 14c, the contributions from a similar lobe centered at $q_y = -q_\psi$ have been neglected. Using this result in Eqn. 10 yields the electric field of the signal beam.

$$\frac{E_s(\vec{q},R,t)}{P_0(t)} = -\frac{k_s^2\omega^2}{4\pi R}\chi(\omega_0)\exp\left\{i\left(\vec{k}_s\cdot R - \omega_0 t\right)\right\}P_d(t)$$

$$\circ\, \Re\left[A_{P1}\Phi^{(d,0)}_{P1} + A_{P1}\Phi^{(d,0)}_{P2} + A_T\Phi^{(d,0)}_T + A_D\Phi^{(d,0)}_D\right], \tag{15a}$$

where we used

$$A_{P1,2} = U_\theta H_{\theta P1,2} + U_e H_{eP1,2} \qquad A_T = U_\theta H_{\theta T} + U_e H_{eT} \qquad A_D = U_\theta H_{\theta D}. \qquad (15b)$$

6 Detected LITA Signal

The detected LITA signal using heterodyne detection is then simply the integral of Eqn. 15 over the detection angle where the detector is centered at $\vec{q} = (0, q_\psi, 0)$. In the limit for a small detector, Eqn. 15 multiplied by the detection angle is the LITA signal. In the experiments presented here, homodyne detection is used. The detector measures the intensity of the electric field, i.e. the square of the modulus of Eqn. 15.

$$\frac{\mathcal{L}_{hom}}{P_0^2(t)} = \frac{k_0 \omega^4}{16\pi^2 \cos^2 \psi} |\chi(\omega_0)|^2$$
$$\times \left(A_{P1} \Phi_{P1}^{(d,0)} + A_{P1} \Phi_{P2}^{(d,0)} + A_T \Phi_T^{(d,0)} + A_D \Phi_D^{(d,0)} \right)$$
$$\times \left(A_{P1}^* \Phi_{P1}^{(d,0)*} + A_{P1}^* \Phi_{P2}^{(d,0)*} + A_T \Phi_T^{(d,0)*} + A_D \Phi_D^{(d,0)*} \right) \qquad (16)$$

In Eqn. 16 we used the fact that the driver pulse (≈ 7 ns) is short compared to the inverse Brillouin frequency and it was approximated by a Dirac delta function which eliminated the double temporal convolution over the driver pulse time history.

In the large detector limit the integration over the detection angle can be approximated by infinite integrals. The final result is then

$$\frac{\mathcal{L}_{hom}}{P_0^2(t)} = \frac{k_0^2}{4\pi^2 \cos^2 \psi} |\chi(\omega_0)|^2 \exp \left\{ -\frac{2}{Y^2}\eta^2 - \frac{2}{Z^2}\zeta^2 \right\}$$
$$\times \left[\exp \left\{ -\frac{8\sigma_y^2}{Y^2 \left(Y^2 + 2\sigma_y^2\right)} \left(\frac{c_s t}{2}\right)^2 \right\} [(P_1 + P_2)(T^* + D^*) + (P_1^* + P_2^*)(T + D)] \right.$$
$$+ \exp \left\{ -\frac{8\sigma_y^2}{Y^2 \left(Y^2 + 2\sigma_y^2\right)} (c_s t)^2 \right\} (P_1 P_2^* + P_1^* P_2)$$
$$\left. + (P_1 P_1^* + P_2 P_2^* + TT^* + TD^* + T^*D + DD^*) \right] \qquad (17)$$

12

where $P_1 = A_{P1}\Sigma_{P1}$, $T^* = A_T^*\Sigma_T^*$, etc., and where the symbols $A_{P1,P2,T,D}$ and $\Sigma_{P1,P2,T,D}$ are defined in Eqn. 15b and Eqn. 14d, respectively.

In the absence of beam misalignments and fluid velocities, Eqn. 17 collapses to the solution in Ref. [4] with the exception of a multiplicative constant. This difference is due to the fact that variations in the x-direction were dropped much earlier than in Ref. [4].

In the absence of bulk fluid velocities, only the misalignment $\overline{\eta}$ changes the time history of the LITA signal whereas η, ζ, and $\overline{\zeta}$ simply decrease the signal intensity. Also, Eqn. 17 is symmetric w.r.t. all possible misalignments. In the absence of beam misalignments, both fluid velocities have a similar influence on the signal that resembles additional acoustic damping and thermal diffusion. Among all misalignment and velocity components, $\overline{\eta}$ and v are the most interesting. In particular by introducing a known $\overline{\eta}$ it is possible to measure the time it takes the density grating to travel to the interrogation beam, thereby obtaining the velocity component v more precisely than by means of an enhanced decay rate. Fig. 2 shows how intentionally misaligning the beans can produce a dependence of the signal on velocity that is more orthogonal to other parameters and therefore more accurately inferred from signals. Note that oscillations are still present in the signal so that the sound speed can also be measured. Depending on the range of velocities to be measured, suitable values for $\overline{\eta}$, ω, and θ can be chosen.

7   Experimental Setup

Figure 3 depicts a schematic diagram of the experimental setup. A Q-switched, frequency-doubled Nd:YAG laser (Spectra Physics, GCR-150-10) drives a dye laser emitting $\sim$ 10-mJ, 7-ns pulses at 589 nm with a repetition rate of 10 Hz. Behind iris $i2$, beam splitter bs splits the beam in approximately equal-intensity halves. Beam splitter bs and mirrors $m3$, $m4$, $m5$ are placed to match the path length of the two beams within $\sim$ 1 mm. Lens $l2$ with focal length of 750 mm focuses both beams onto the sample volume in the test section. Lens $l2$ and mirror $m6$ are mounted on a translation stage with a 10-μm-resolution micrometer drive. The test section is a high-pressure
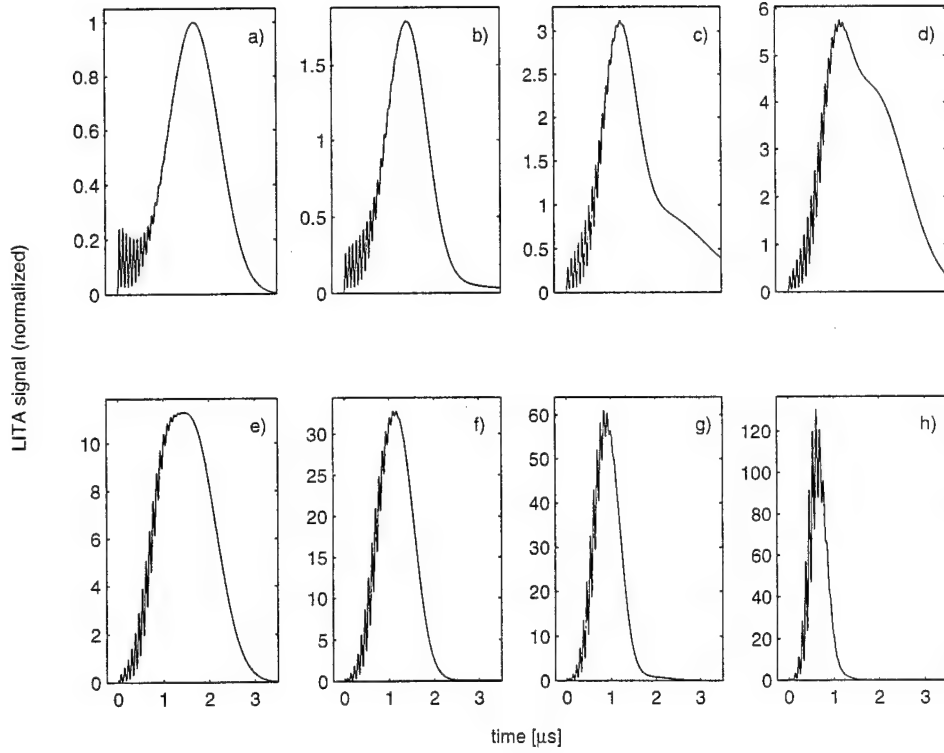
Figure 2: Theoretical LITA signals for atmospheric air from Eqn. 17 with $\theta = 1.23°$, $\omega = 370$ μm, $\sigma = 700$ μm, misalignment $\overline{\eta} = -2\omega$ and with in fluid flow in y-direction with different Mach numbers; a) $M = 0$, b) $M = 0.25$, c) $M = 0.5$, d) $M = 0.75$, e) $M = 1.0$, f) $M = 1.5$, g) $M = 2.0$, h) $M = 3.0$.
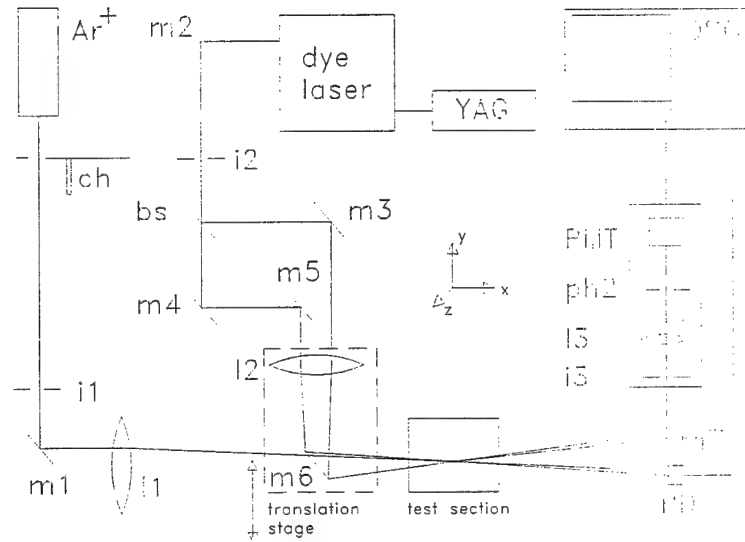
Figure 3: Schematic diagram of experimental LITA setup.

bomb with optical access via anti-reflective coated BK7 windows on opposite sides.

A CW Argon-ion laser (Spectra Physics, Model 165) at 488 nm provides 0.5 W for the source beam. A chopper wheel ch (Scitech Instruments, Optical Chopper) blocks the beam except for pulses of 1-ms duration which are synchronized (LabSmith LC880) with the Q-switch trigger of the Nd:YAG laser. As with the driver laser, iris $i1$ partially removes unwanted beam modes, and lens $l1$ (f=1 m) focuses the beam onto the sample volume. The beam passes just over mirror $m6$ which directs the driver beams into the test section. Note that this optical setup introduces a small angular beam misalignment with $\phi_1 = \phi_2$. Mirror $m7$ directs the scattered beam through iris $i3$ into the receiver unit where it is focused on and passed through pinhole ph with a diameter of 400 μm.

The signal beam is detected by a photomultiplier tube (Hammamatsu model OPTO-8) and recorded on a digital storage oscilloscope (Tektronix, TDS 640A) from which it is transferred over an IEEE 488 bus to a personal computer for data analysis. The transmitted part of the source

15

(interrogation) beam is blocked as is one of the two driver beams exiting the test section. The other is detected by photo detector PD (Thor Labs, DET-2SI) and used to trigger the data acquisition. Each signal contains 2,000 data points taken at a sampling rate of 500 MS/s.

8   Procedure

For all experiments presented here, the test section was filled with atmospheric air seeded with NO_2 at concentrations on the order of parts per million. The low level of seeding enhances the signal level by typically two orders of magnitude without changing the results of the measurements. Also, this seeding makes thermalization predominant over electrostriction which can therefore be ignored.

For the data analysis, a standard personal computer (Pentium, 150MHz) is used to find the least-squares fit of a theoretical signal (Eqn. 17) to an experimental trace. To keep the number of floating fitting parameters as low as possible, values for the beam diameters ω and σ, beam crossing angle θ, etc. are obtained from a set of calibration measurements. A Levenberg-Marquart scheme is used for the least-squares fit, which is a combination of the inverse Hessian (multidimensional form of Newton's method) scheme and the method of steepest descent (Ref. [9]).

Eqn. 17 was validated by moving the translation stage with lens $l2$ and mirror $m6$ in the y-direction, thus creating a known misalignment $\bar{\eta}$. The measurement started at a value of $\bar{\eta} = -2$ mm and a trace was recorded every 10 μm until reaching $\bar{\eta} = +2$ mm. Every trace was averaged over 64 driver-laser shots to reduce the noise levels at larger misalignments.

For these measurements in which the correct beam misalignment was to be inferred from the signal shape, only the misalignment component in question and U_θ, the thermal grating modulation depth, were adjusted during the numerical fit. The latter parameter had to be included to serve as a multiplicative factor since Eqn. 17 cannot accurately give the absolute signal but rather a relative time history whose total amplitude depends additionally on the characteristics of the detector and other factors.

16

In a second set of measurements, we wanted to find whether small beam misalignments affect the repeatability and/or accuracy of LITA measurements. This was of particular interest since it did not seem not possible to detect such misalignments by the fitting procedure. Hence, at a number of fixed beam misalignments $\overline{\eta}$, 500 64-shot averages were obtained as data for a statistical analysis. Here, only the sound speed, thermal diffusivity, and U_θ where adjusted during the fitting procedure. These data sets were analyzed three different ways: first, with all misalignments (wrongly) set to zero, secondly with the misalignments held fixed at their correct values, and finally with the misalignment $\overline{\eta}$ set as a fitting parameter during the data analysis.

9   Results, Discussion

Fig. 4 shows LITA signals recorded with various misalignments. For large values of $\overline{\eta}$ (Fig. 4a & b), the only visible signal is due to an isolated acoustic wave passing through the source beam. We see that the onset of the signal has a steeper slope than the tail, a result of acoustic damping. Beam diameters can be inferred accurately from these traces. The width of the hump in the signal gives a good measure of the driver beam width ω. In the absence of acoustic damping, the deviation of the exact shape of the signal from a Gaussian profile gives information about the source beam diameter σ. But, since Γ is known in these experiments, this information can still be determined using the least-squares fit to Eqn. 17.

In Fig. 4c we see the first oscillations in the signal. This indicates that at this location there is a sizable overlap of the source beam with both the thermal grating and the acoustic waves. As $\overline{\eta}$ is decreased further, the hump moves to earlier times and the oscillations become stronger. Note the subtle change in signal shape between Figs. 4e & f considering the large step in $\overline{\eta}$.

Fig. 5 shows an experimental LITA signal together with the result of the fitting procedure. For clarity, they are plotted separately. We see how precise Eqn. 17 captures the features of a misaligned signal.

Fig. 6 shows the beam misalignment inferred by the fitting routine vs. the actual misalignment
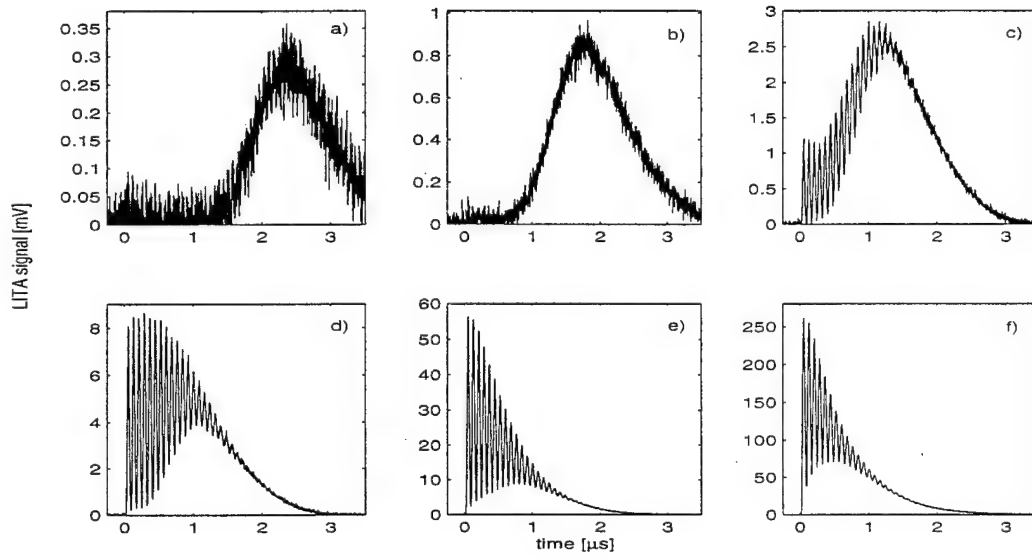
Figure 4: LITA signals of atmospheric air, $\sigma = 700$ μm, $\omega = 370$ μm, $\theta = 1.23°$, and: a) $\bar{\eta} = 1100$ μm, b) $\bar{\eta} = 900$ μm, c) $\bar{\eta} = 700$ μm, d) $\bar{\eta} = 600$ μm, e) $\bar{\eta} = 500$ μm, f) $\bar{\eta} = 0$ μm.
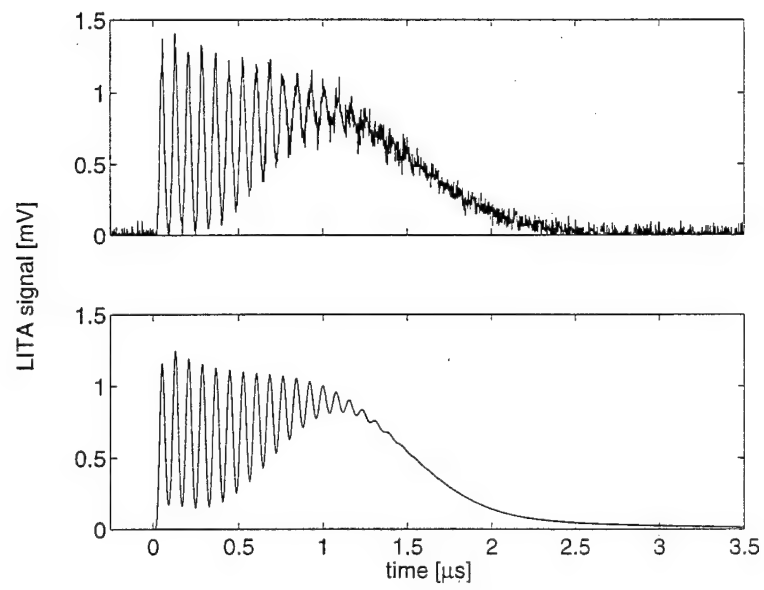
Figure 5: Experimental signal (top) and fitted theoretical signal (bottom) for $\overline{\eta} = 500$ μm with $\omega = 370$ μm, $\sigma = 700$ μm, $\theta = 1.23°$ in atmospheric air.

19

set by the translation stage. The dashed lines with a slope of ± 1 correspond to the ideal case. For $\overline{\eta} > 550$ μm, the extracted values for $\overline{\eta}$ had the correct slope but were generally too large by about 200 μm. For very large values of $\overline{\eta}$, the larger scatter in the measurements is due to the increased noise level in the signals. A linear regression for the region $|\overline{\eta}| > 600$ μm gives slopes in these regions of $m = -.946$ and $m = 0.995$, respectively, with a coefficient of determination, r^2, greater than 0.98. The standard error for the measured $\overline{\eta}$ is 22 μm.

In the center region, the detected misalignment forms a plateau at 300 μm. The reason for this behavior is probably that the intensity profiles of the beams in the experiments are not well represented by Gaussians. Fig. 7, which shows the peak signal intensity vs. $\overline{\eta}$, also provides evidence that this assumption is not satisfied. If we give the fitting routine the option of an additional fitting parameter whose effect on the signal depends strongly on the beam profiles, e.g., misalignment, while not accurately modeling the beam profiles, it is unlikely that the fitting routine will return the proper value of the parameter.

The dashed line in Fig. 7 represents the theoretical value of the (visible) peak intensity. The intensities are normalized with the intensity at $\overline{\eta} = 0$. First, consider the theoretical curve in which we can distinguish three regimes.

For $|\overline{\eta}| < 650$ μm (regime I) we find a Gaussian behavior for the signal intensity w.r.t. $\overline{\eta}$. Here, the peak value occurs early on in the LITA signal (Figs. 4e & f) due to constructive interference of the thermal grating with the acoustic waves. Both gratings have a Gaussian profile so the peak intensity scales the same way.

In regime II (650 μm $\leq |\overline{\eta}| \leq$ 1300 μm) the peak intensity occurs at later times in the signal when an isolated acoustic wave passes the interrogation beam (Figs. 4a & b). The travel time of the wave scales linearly with the misalignment. The wave's amplitude decreases exponentially with the acoustic damping rate Γ. This explains the linear behavior on a logarithmic plot for large misalignments in Fig. 7. Figs. 4c & d mark the transition between these two regimes.

For $|\overline{\eta}| > 1300$ μm (regime III) the theoretical signal intensity decreases again faster than in region II. This is an artifact of the limited duration of the data acquisition. In this regime, the
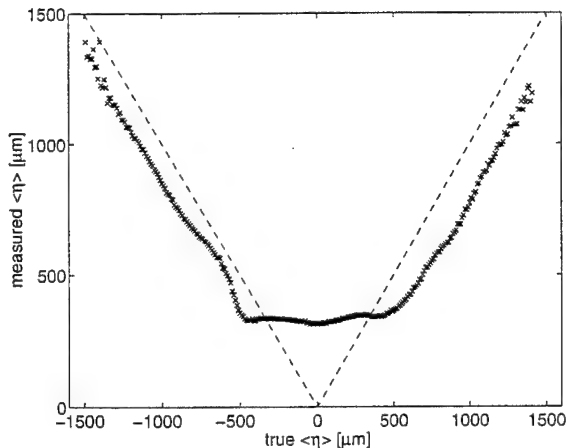
Figure 6: Measured vs. true misalignment $\bar{\eta}$. The dashed lines have a slope of ± 1 respectively. The experimental conditions are the same as in Fig. 4.
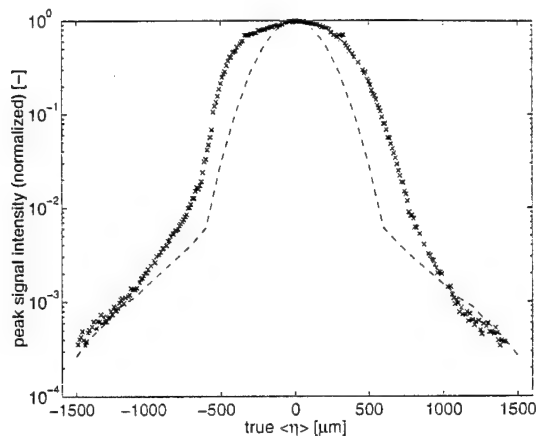
Figure 7: Normalized peak signal intensity vs. $\bar{\eta}$. The experimental conditions are the same as in Fig. 4.

peak of the hump visible in Figs. 4a & b occurs after the end of the recording time.

The measured peak intensities are higher than predicted over a range of misalignments near perfect alignment before they approach the theoretical values at larger $\bar{\eta}$. The most likely explanation is the presence of laser modes other than TEM_{00}. We can see the transition from regime I to regime II in Fig. 7. The transition to III is less pronounced as at this point signals are very weak. We can see the effect of noise from the large amount of scatter in the intensities in Fig. 7.

As evidenced by Fig. 6 it was not possible to extract accurate measurements of small misalignments from the signal shape. This finding prompts the question of whether small misalignments have an impact on the accuracy and uncertainty of other LITA measurements. Figs. 8a & b respectively show the uncertainty and the accuracy of LITA measurements of sound speed vs. $\bar{\eta}$ for the three different fitting strategies.

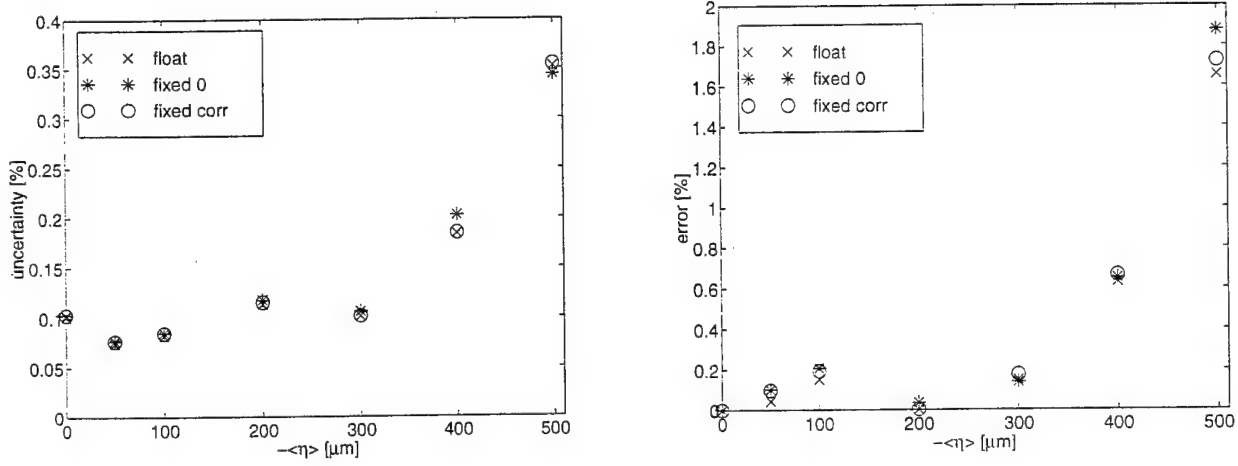All three fitting strategies yield almost identical results. For $|\bar{\eta}| \leq 300$ μm the uncertainty

Figure 8: Uncertainty and error of sound speed vs. $\overline{\eta}$. The sound speed for $\overline{\eta} = 0$ is taken as reference. Three different fitting strategies were used. In the strategy denoted by "float," $\overline{\eta}$ is a floating fitting parameter, in "fixed 0," $\overline{\eta}$ is fixed at zero, and in "fixed corr," $\overline{\eta}$ was held constant at the correct preset value. The experimental conditions are the same as in Fig. 4.

22

remains approximately constant at 0.1% as does the error of 0.2%, where the measured sound speed from the data set with $\overline{\eta} = 0$ has been taken as reference value. Only for $|\overline{\eta}| > 300$ μm do the uncertainty and error increase significantly.

Other types of misalignments that have been carried out experimentally include measurements where only one driver beam was displaced in y-direction, thus inducing a simultaneous misalignment in $\overline{\eta}$ and η; moving both beams in opposite directions (only η) and measurements with misalignments in the z-direction, i.e., sweeps through $\overline{\zeta}$ and ζ. Misalignments in the y-direction produced similar results to those explained in detail above. For nonzero values of ζ or $\overline{\zeta}$, no change in signal shape has been observed as Eqn. 17 predicts.

When a small-diameter, 40 μm pinhole ph was used in the receiver unit, another form of misalignment was observed that is not included in Eqn. 17. Changes in signal shape did not appear to be symmetric w.r.t. $\overline{\eta}$. The most likely explanation for this asymetry is that part of the signal beam was occluded by the pinhole. An illustration of this effect is shown in Fig. 9. In the upper half we see the intensity of the overlap of the density grating with the source beam in physical space along the y-axis as it develops over time. The bright and dark stripes correspond to the oscillations in the early stages of the signal whereas the bright tail reflects the exponentially decaying tail of the LITA signal.

In the large detector limit we assume that the detector integrates over the entire horizontal range in Fig. 9 (and beyond). Imagine that half of the signal beam is blocked so the receiver sees only the left or right half of the signal beam (receiver misalignment). The resulting LITA signals are given in the lower half of Fig. 9. We see that for $\overline{\eta} = 0$ this has no influence on the signal shape. In fact, we could take any region along the y-axis and would end up with the same signal shape, meaning that this kind of misalignment cannot be detected if the optics are otherwise perfectly aligned.

However, if $\overline{\eta} \neq 0$, then the time histories at different positions y are no longer self similar, resulting in different signals depending on which part of the signal beam the detector sees.

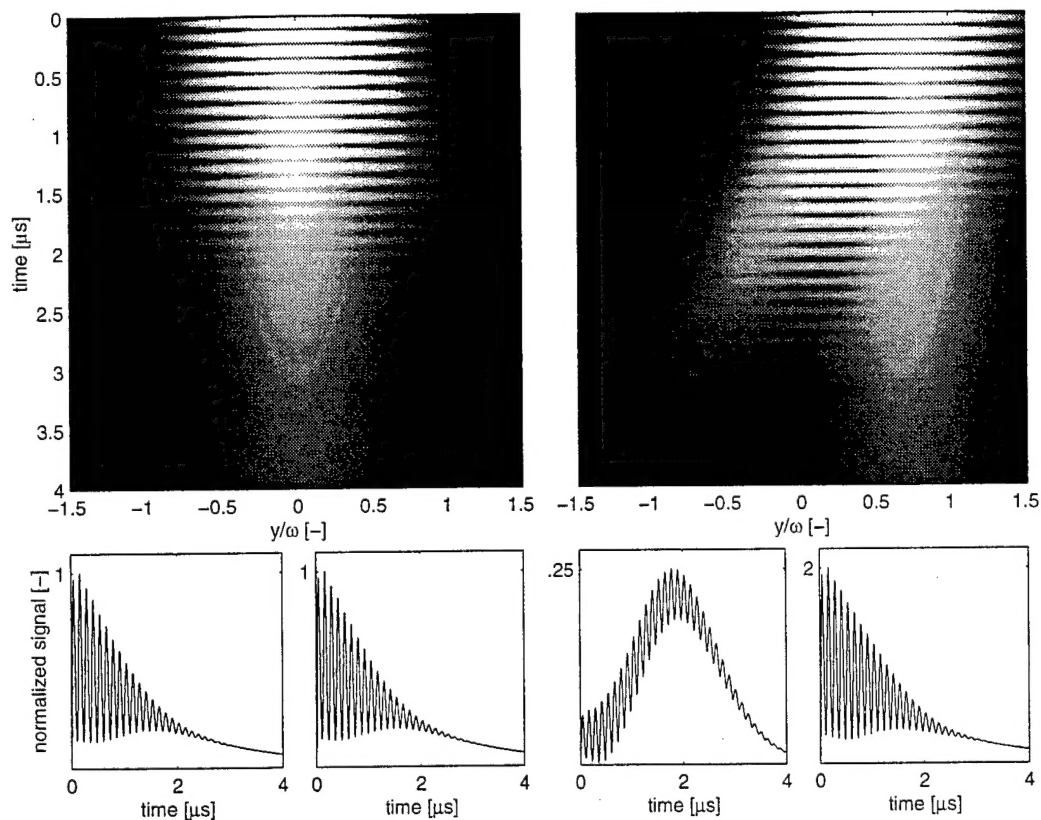Figure 10 provides evidence that detector misalignment produces asymmetry in beam-misalignment

23

Figure 9: Intensity of overlap of density grating with source beam from the inverse Fourier Transform of Eqn. 14 for atmospheric air and at $z = 0$, i.e., along the grating center line. On the top, the time history as a function of y-position is plotted - on the left for perfect beam alignment, on the right with $\bar{\eta} = \omega$. The experimental parameters are: $\sigma = \omega = 500$ μm, $\lambda_d = 589$ nm, $\theta = 0.8°$. White corresponds to high intensities, black to low intensities. In the lower portion, the resulting LITA signals are shown if the receiver only detects the range $y < 0$ or only $y > 0$, respectively.
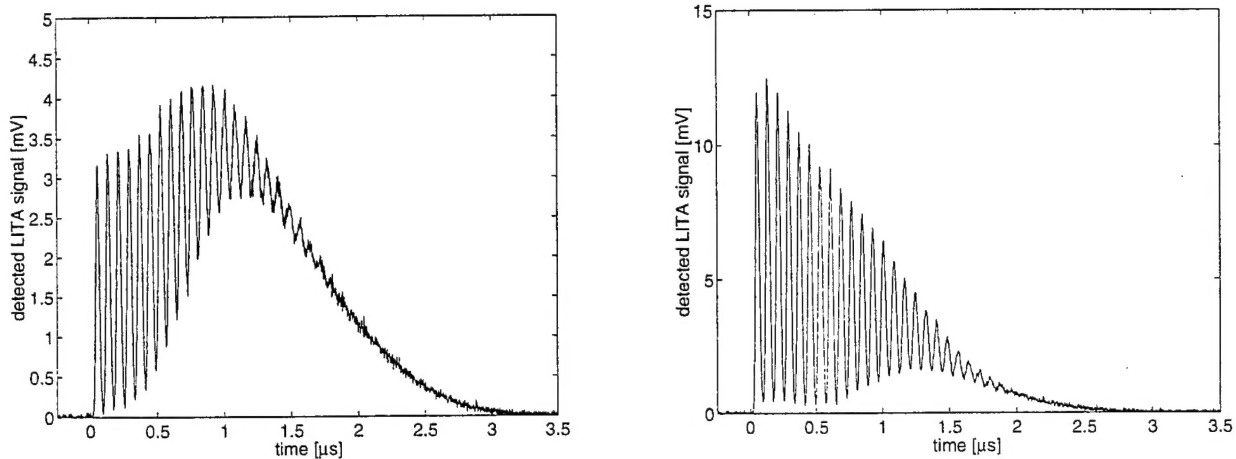
Figure 10: Two traces from a sweep through values of $\bar{\eta}$. Left trace: $\bar{\eta} = -650$ μm; right trace: $\bar{\eta} = +650$ μm. A small pinhole ph with a diameter of only 40 μm in the receiver unit blocked portions of the signal beam. Compare with theoretical results in Fig. 9.

effects. Here, two traces taken at $\bar{\eta} = \pm 650$ μm are shown from earlier measurements with the 40 μm pinhole. We clearly see the difference in the signal shape. Compare Fig. 10 with the two traces in the lower right of Fig. 9.

To fully verify the origin of the asymmetry, we performed a series of measurements using the 40-μm pinhole in which, for several values of $\bar{\eta}$, the mirror $m7$ was translated to block different regions of the signal beam. The influence of receiver misalignment on the signal shape was demonstrated, but since this form of misalignment is not included in Fig. 17, no quantitative data can be given. Subsequently, the use of a larger size pinhole eliminated the asymmetry at the cost of increased sensitivity to incoherently scattered light and luminosity.

Finally, consider the case of angular beam misalignments and misalignments in the x-direction. Both can produce a rotation of the principal axes of the grating structure. As a consequence, the phase matching condition for the source beam may no longer be satisfied resulting in a weaker signal beam that may even be scattered into a different direction than anticipated. This alone,

however, does not change the shape of the signal as long as the entire signal beam falls on the detector.

10   Conclusions

An analytical expression for the magnitude and time history of LITA signals from finite Gaussian beams in the presence of fluid velocities and the most common forms of beam misalignment has been derived. In experiments, some deviations from this expression were observed that were due to non-Gaussian laser beam profiles. In regions where this assumption was satisfied however, the experiments showed very good agreement with the theory.

It was demonstrated how beam misalignment can be detected quantitatively only from the shape of the signal. Small misalignments that could not be accurately measured were shown not to influence the accuracy or repeatability of sound speed measurements, even when the data analysis incorrectly assumed that no misalignments were present during the measurement.

Controlled beam misalignments may be advantageous for optimizing the accuracy of measurements of a particular parameter. For example, beam misalignments can improve the accuracy of homodyne LITA velocimetry.

11   Acknowledgements

References

[1] T.J. Butenhoff, *Measurement of the thermal-diffusivity and speed of sound of hydrothermal solutions via the laser-induced grating technique*, Intl. J. Thermophys. v16 (1), pp1-9 (1995)

[2] D.J.W. Walker, R.B. Williams, P. Ewart, *Thermal grating velocimetry*, Opt. Letters 23:(16), 1316-1318, 1998

[3] R.B. Williams, P. Ewart, A. Dreizler, *Velocimetry of gas-flows using degenerate 4-wave mixing*, Opt. Letters v19 (18), 1486-1488 (1994)

[4] E. B. Cummings, I. A. Leyva, H. G. Hornung, *Laser-induced Thermal Acoustics (LITA) Signals from Finite Beams*, Appl. Opt. Vol. 34, No. 18 (1995).

[5] H. J. Eichler, P. Günther, D. W. Phol, *Laser-Induced Dynamic Gratings*, Springer-Verlag, New York, 1986.

[6] D.B. Brayton: Appl. Opt. 13, 2346 (1974)

[7] A.E. Siegman: J. Opt. Soc. Am. 67, 545 (1977)

[8] B.J. Berne, R. Pecora, *Dynamic Light Scattering*, John Wiley & Sons, New York, 1976

[9] W. H. Press, *Numerical Recipes in C: The Art of Scientific Computing*, Cambridge University Press, 1988.